High-transverse-momentum single-hadron production in pp and pd collisions at $\sqrt{s}$ = 27.4 and 38.8 GeV

D. E. Jaffe,[h,*] P. B. Straub,[i] M. R. Adams,[h,*] C. N. Brown,[d] G. Charpak,[b] W. E. Cooper,[d] J. A. Crittenden,[c,†] D. A. Finley,[d] H. D. Glass,[h,‡] R. Gray,[i,§] Y. Hemmi,[g] Y. B. Hsiung,[c,**] J. R. Hubbard,[a] A. M. Jonckheere,[d] H. Jöstlein,[d] D. M. Kaplan,[e,††] L. M. Lederman,[d] K. B. Luk,[i,**] A. Maki,[f] Ph. Mangeot,[a] R. L. McCarthy,[h] K. Miyake,[g] R. E. Plaag,[i,‡‡] J. P. Rutherfoord,[i,§§] Y. Sakai,[f] J. C. Santiard,[b] F. Sauli,[b] S. R. Smith,[c] T. Yoshida,[g] and K. K. Young[i]

[a]*CEN Saclay, Gif-sur-Yvette, 91190 France*
[b]*CERN, CH-1124 Geneva, 23 Switzerland*
[c]*Columbia University, New York, New York 10027*
[d]*Fermilab, Batavia, Illinois 60510*
[e]*Florida State University, Tallahassee, Florida 32306*
[f]*KEK, Tsukuba, Ibaraki-ken, 305 Japan*
[g]*Kyoto University, Kyoto, 606 Japan*
[h]*State University of New York, Stony Brook, New York 11794*
[i]*University of Washington, Seattle, Washington 98195*

(Received 20 March 1989)

Results of high-transverse-momentum charged-hadron production in 400-GeV/c proton-proton and proton-deuteron collisions and 800-GeV/c proton-proton collisions are presented. The transverse-momentum range of the data is from 5.2 to 9.0 GeV/c for the 400-GeV/c collisions and from 3.6 to 11.0 GeV/c for the 800-GeV/c collisions; the data are centered around 90° in the proton-nucleon center-of-momentum system. Single-pion invariant cross sections and particle ratios were measured at both energies. The results are compared to previous experiments and the Lund model.

I. INTRODUCTION

Since the first observations at the CERN Intersecting Storage Rings (ISR), large-transverse-momentum (p_T) hadrons produced in proton-nucleon collisions have been a fruitful source of data on the parton constituents of hadrons. They have also been shown[1] to carry substantial fractions of the momenta of their parent constituents. Thus the study of high-p_T pion production can elucidate the interaction mechanism of the constituents of the nucleon. To this end, high-p_T charged-pion production has been investigated at Fermilab[2] and the CERN ISR.[3]

In addition the quantum numbers of high-p_T hadrons have been shown to be correlated with the flavor of the scattered parton.[1,4,5] The measurement of the relative production rates of charged pions, kaons, and protons provides insight into the structure of the nucleon and the subsequent fragmentation of the struck partons. The measurements of this experiment are compared with the Lund Monte Carlo predictions for high-p_T hadron production,[6] which has successfully modeled inclusive meson and baryon production in electron-positron interactions.[7]

This paper presents results of charged-hadron production near 90° in the proton-nucleon center-of-momentum system (c.m.s.) in pp collisions at $\sqrt{s}$ = 27.4 and 38.8 GeV and pd collisions at $\sqrt{s}$ = 27.4 GeV taken in the Meson East beam line at Fermilab. Table I displays the ranges in p_T, $x_T = 2p_T/\sqrt{s}$, and c.m.s. production angle (Θ^*) examined.

TABLE I. The reactions and kinematic ranges of the data.

Reaction	$\sqrt{s}$ (GeV)	p_T range (GeV/c)	$x_\perp$ range	cos Θ^* range
$pp(d) \rightarrow hX$	27.4	5.2–9.0	0.38–0.66	−0.3 to 0.3
$pp \rightarrow hX$	38.8	3.6–11.0	0.19–0.57	−0.2 to 0.2

II. APPARATUS AND DATA ANALYSIS

A. Overview

Experiment 605 (E605) at Fermilab[8–10] was based upon a focusing magnetic spectrometer designed to study long-lived, charged, high-p_T particles near 90° in the proton-nucleon center-of-momentum system produced in 400- and 800-GeV/c proton-nucleus collisions. See Fig. 1. Tracking information was provided by six planes of multiwire proportional chambers at station 1 and six planes of drift chambers at stations 2 and 3. Charged pions, kaons, and protons were identified with a ring-imaging Cherenkov counter. Electrons were differentiated from hadrons by calorimetry, and muons were identified by scintillation-counter hodoscopes and proportional tubes behind more than 20 absorption lengths of dense shielding.

An important modification to the E605 spectrometer,

 ©1989 The American Physical Society

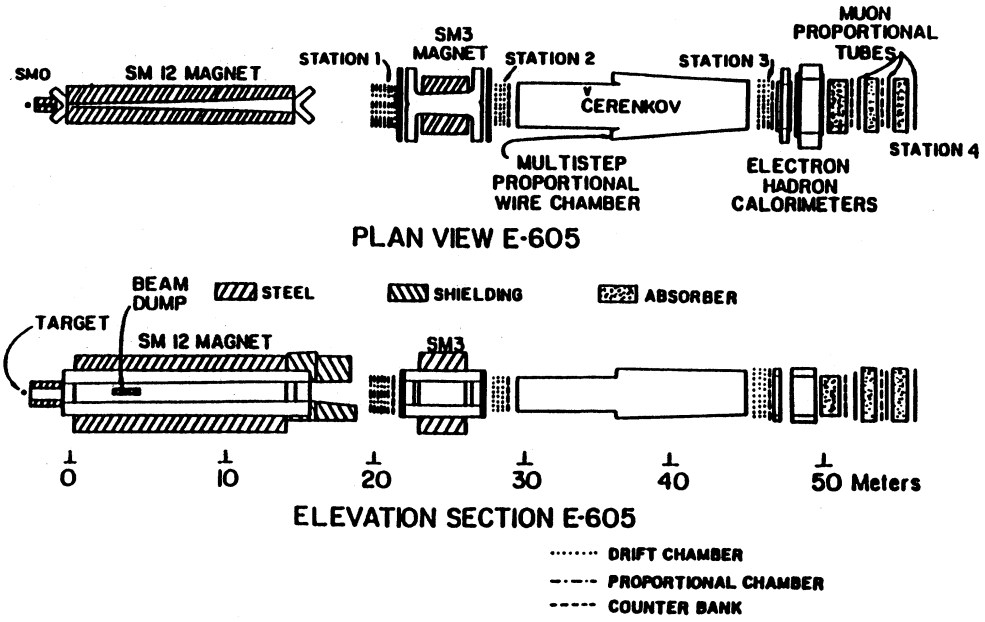

FIG. 1. The E605 spectrometer.

described in detail in Ref. 9, was the repositioning of the target upstream to accommodate an additional spectrometer magnet (SM0) and a low-angle, tungsten collimator. In addition a series of lead-tungsten baffles were installed in the large SM12 magnet as shown in Fig. 2. For these data, SM0, SM12, and SM3 had transverse-momentum kicks of approximately 1.3, 7.5, and 0.9 (0, 7.5, and -0.9) GeV/c, respectively, for the 400- (800)-GeV/c data. These modifications increased the high-p_T acceptance and reduced the backgrounds in the rest of the apparatus.

B. Beam and target

A 400- or 800-GeV/c proton beam struck a cylindrical target vessel with 25-μm stainless steel walls, 5.08 cm in diameter, and 20.2 cm along the beam filled with either liquid hydrogen (LH_2) or deuterium (LD_2). The beam profile at the target was determined to be roughly Gaussian in both the vertical (Y) and horizontal (X) directions with a vertical root-mean-square (rms) width of 0.19 mm and a horizontal rms width of about 2.3 mm (Ref. 11). The magnetic field of the spectrometer magnets was in the X direction so that charged particles were bent vertically. The LH_2 used in the target was measured[12] to be $>99.99\%$ pure; the two different batches of liquid deuterium used were found to be 98.5% D_2, 1.5% HD, and 95% D_2; 5% HD (percent by volume), respectively. No correction was applied to the measurement of the single-pion cross section to account for the slight hydrogen contamination of the "deuterium" target resulting in a systematic uncertainty in the pd cross section of $\pm 2.0\%$ (limit of error). To correct the cross section for secondary particle production in the target vessel, one empty-target run was taken for about every three (four) LH_2 (LD_2) data runs. The correction applied was less than 2% for all values of p_T.

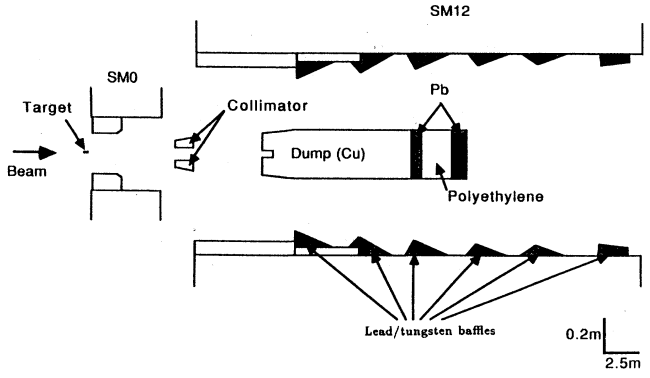

FIG. 2. Enlarged view of SM0 and SM12 showing the tungsten collimator and lead-tungsten baffles.

The beam intensity was monitored by a secondary-emission monitor (SEM) calibrated by foil activation once during each of the 400- and 800-GeV/c running periods. The results of the calibration were $(8.14 \pm 0.31) \times 10^7$ and $(8.52 \pm 0.53) \times 10^7$ protons on target per SEM count for the 400- and 800-GeV/c running periods, respectively. Table II lists the total integrated luminosity for each data

TABLE II. The total number of protons on target and integrated luminosity for each data set. Only statistical uncertainties are shown in the table; the $\pm$ 2% (limit of error) systematic uncertainty in the pd luminosity is not shown.

Data set	Total protons on target	Integrated luminosity per target nucleus (pb^{-1})
400 GeV pp	$(5.09 \pm 0.19) \times 10^{14}$	436±23
400 GeV pd	$(7.80 \pm 0.29) \times 10^{14}$	761±39
800 GeV pp	$(7.17 \pm 0.45) \times 10^{14}$	615±32

set. In addition, a four-counter telescope pointed at the target perpendicular to the incident beam monitored the interaction rate in the target.

C. Hadron-species identification

Hadron identification was achieved using a large-aperture ring-imaging Cherenkov detector.[10,13,14] Photons emitted in a 15.2-m-long radiator of ultrapure helium reflected off a 4×4 array of mirrors onto two multistep proportional wire chambers. The ring radius for the highest-momentum track was 70 mm. The ring radius resolution is about 1 mm, primarily due to the chromatic dispersion of the helium. Using samples of high-momentum muons, several detector parameters were tabulated for each run. These include the index of refraction and chromatic dispersion of the helium, the number distributions of reconstructed signal and noise photons for each track, and the orientation of the mirrors. For each hadron track, this information was used to calculate the likelihood for the reconstructed photon pattern to be produced under each of the three hadron hypotheses. For a track with n photons, the likelihood was a probability density over the n photon positions. A typical high-momentum pion had 2.2 reconstructed photons on the ring. There were typically 1.6 noise photons reconstructed within 85 mm of the ring center. Thus for each track, the likelihoods L_i^α were computed (greek indices run over π, K, and p, and i is the track index). For an ensemble of N tracks in a given kinematic bin, the hadron fractions f_π, f_K, and f_p ($\sum_\alpha f_\alpha = 1$) were determined by solving the likelihood equations

$$f_\alpha = \sum_{i=1}^{N} \frac{L_i^\alpha f_\alpha}{\sum_\beta L_i^\beta f_\beta} .$$

D. Triggering

The single-hadron trigger employed two elements—a high-speed, hardware look-up table (the "trigger matrix") and a calorimeter energy signal—described in an earlier paper.[9]

For these data, the trigger matrices contained the combinations of hodoscope counters in stations 1, 2, and 3 corresponding to a particle trajectory from the target through the upper ("*YU*") and lower ("*YD*") aperture of the SM12 magnet. The logical OR of these two signals formed the "*Y*" trigger element.

Two calorimeter total-energy signals were formed (1) a high-threshold signal, dubbed "*EHI*," and (2) a lower-threshold signal, dubbed "*ETFI*." In addition energy sums corresponding to localized deposits in the upper ("*EU*") or lower ("*ED*") portion of the calorimeter were formed and combined with "*YU*" and "*YD*," respectively, to form a trigger designed to accept single high-p_T hadrons.

For the 400-GeV/c data, the $EU \cdot YU$ and $ED \cdot YD$ triggers were used in combination with *ETFI*, prescaled to an acceptable rate, and *EHI*. In the 800-GeV/c run, the $EHI \cdot Y$ trigger was substituted for the *EHI* trigger. The low-threshold *ETFI* trigger was essential in determining the efficiencies of the *EU*, *ED*, and *EHI* triggers as described in the next section.

E. Yield correction

These data were subjected to an analysis technique similar to that described in an earlier paper.[9] The following describes the corrections applied to these data.

1. Monte Carlo simulation

A simpler Monte Carlo program was used for the analysis. This Monte Carlo program determined the geometrical acceptance for each p_T bin by using the same magnetic-field map and aperture cuts in the data analysis. The geometrical acceptance is defined as the fraction of particles produced in a given kinematic bin whose trajectories pass through the experimental aperture. Figures 3(a)–3(d) show the calculated geometrical acceptance for the upper and lower apertures of the SM12 magnet for the $\sqrt{s}$ =27.4- and $\sqrt{s}$ =38.8-GeV data. The difference between the upper and lower apertures $\sqrt{s}$ =27.4 GeV acceptance at high p_T was due to the misalignment in Y of the target and the SM12 magnet— the magnet's immense weight caused it to sink slightly. This small effect was reduced for the $\sqrt{s}$ =38.8-GeV data by running SM12 and SM3 with opposing magnetic fields.

Instead of incorporating the efficiencies of the various detector elements into this simple Monte Carlo simulation, the efficiencies of each detector element were determined from data taken concurrently with the less restrictive *ETFI* trigger. Three factors in the hadron yield were affected by this technique: the tracking efficiency, the hodoscope efficiency, and the calorimeter trigger efficiency.

2. Tracking efficiency

The tracking efficiency was calculated from the individual wire-chamber efficiencies and the track-finding algorithm. The calculated tracking efficiency varied between 91% and 96%. The systematic uncertainty in the tracking efficiency was estimated by recalculating the tracking efficiency while varying the wire-chamber efficiencies by one standard deviation using the calculated statistical uncertainties in the wire-chamber efficiencies.

3. Hodoscope efficiency

At least four of the five hodoscopes intersected by the reconstructed track in stations 1, 2, and 3 were required to fire. This cut ensured that the track satisfied the trigger requirement. The average efficiency of each hodoscope was measured to be 97%.

4. Calorimeter trigger efficiency

A more complex technique[11,14,15] was used to determine the calorimeter trigger efficiencies and their respective uncertainties. A calorimeter trigger was generated each time the total pulse height of the phototube dynode signals exceeded a set threshold. In the data analysis, the

pulse height PH associated with a reconstructed track is

$$\mathrm{PH}=\sum_m a_m Q_m f(x) ,$$

where the sum extends over the calorimeter modules near the track that were included in the hardware trigger, $f(x)$ corrects for light attenuation in the scintillator, Q_m is the charge recorded for module m in the analog-to-digital converters, and a_m represents the fact that pulse shapes can differ from module to module. The factors a_m and $f(x)$ are constructed so that the calculated PH threshold does not depend on the track position at the

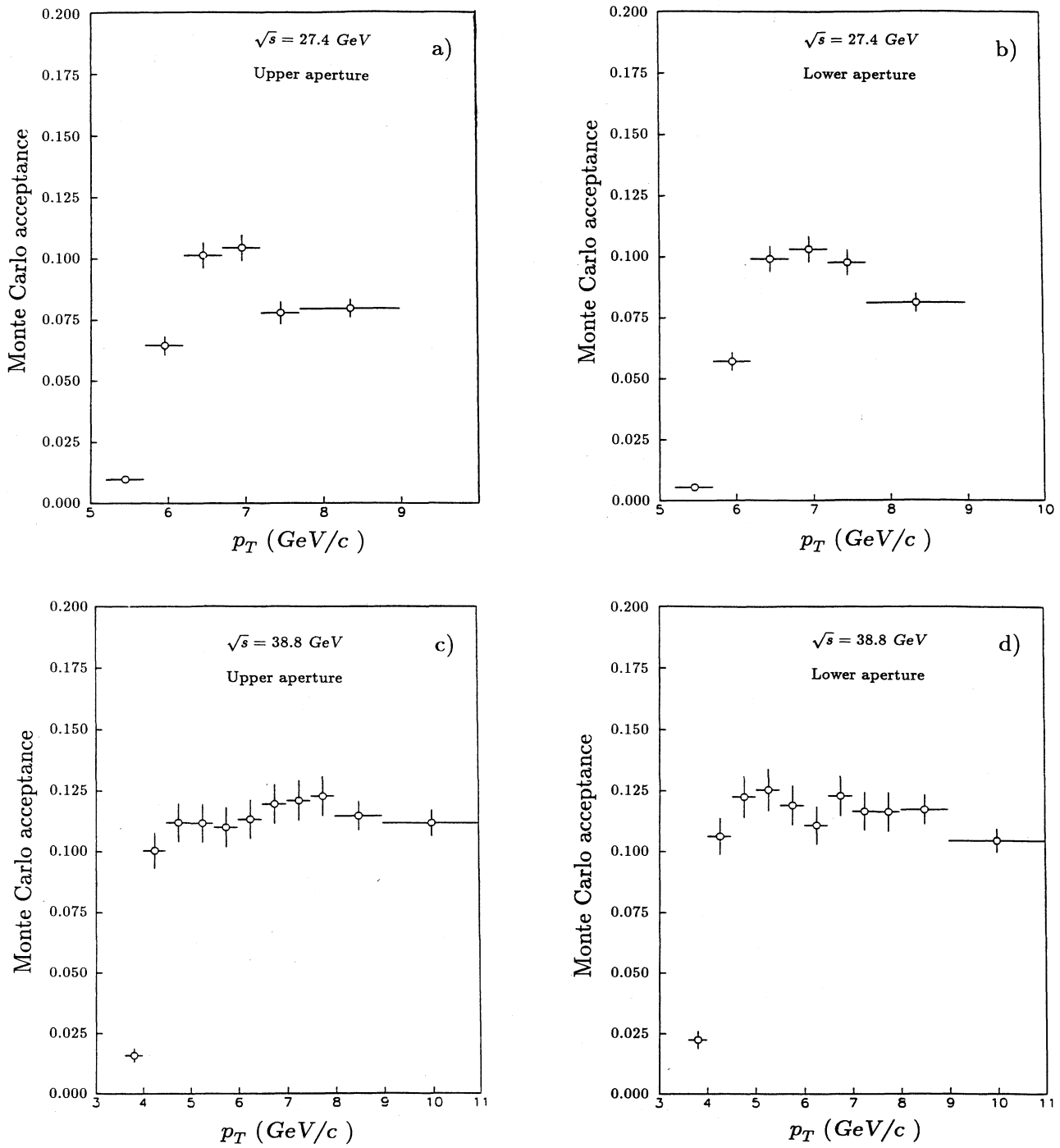

FIG. 3. The calculated geometric acceptance as a function of transverse momentum for the (a) upper and (b) lower apertures for the $\sqrt{s}$ =27.4-GeV data and for the (c) upper and (d) lower apertures for the $\sqrt{s}$ =38.8-GeV data. The horizontal error bars show the width of the transverse-momentum bin; the vertical error bars indicate the statistical uncertainty of the Monte Carlo results.

calorimeter. The calorimeter efficiency ϵ (PH) is defined as the number of times a trigger fired in coincidence with the lower-threshold *ETFI* trigger normalized by the number of times the *ETFI* trigger fired and was fit with an error function (integral of a Gaussian distribution):

$$\epsilon(\mathrm{PH}) \equiv \mathrm{erf}(\mathrm{PH}; T, \sigma) = \frac{1}{\sqrt{2\pi}\sigma} \int_0^{\mathrm{PH}} dx \, \exp\left[-\left[\frac{x-T}{\sigma} \right]^2 / 2 \right],$$

where T is the "threshold" of the trigger, the mean of the Gaussian. Note that $\epsilon(T)=0.5$, and σ is "jitter" in the threshold, the width of the Gaussian distribution.

The computed efficiency of the *EHI* trigger for the 800-GeV/c data is shown in Fig. 4. The calorimeter trigger efficiency was computed event by event using the PH and the results of the fit to the error function. The systematic uncertainty in the calorimeter trigger efficiency was determined from the estimated uncertainties in the threshold and the jitter of ± 0.5 and $\pm 4.6\%$ (± 1.0 and $\pm 9.2\%$), respectively, for the 800- (400-) GeV/c data.

For the majority of the bins, the systematic uncertainty in the single-pion cross section is dominated by the uncertainty in the calorimeter efficiency. To eliminate bins at the limits of the overall detector acceptance, all events in each bin were required to have an overall efficiency greater than 5%. The average efficiency of the *worst* bin was 37%.

F. Absorption and decay correction

A species-dependent correction was applied to each track to account for the probability of decay in flight or nuclear absorption in the apparatus before the detector could be triggered. The absorption probability in the target and the material upstream of the calorimeter was estimated to be 2.3% with a systematic error of 0.9% due to uncertainties in the exact thickness and composition of the detector materials.

All purely leptonic decay modes of the pion and kaon will not trigger the apparatus, while a negligible fraction (<0.001 at 100-GeV/c momentum) of the nonleptonic decays can both trigger the apparatus and be reconstructed as a target track. At a momentum of 100 GeV/c, approximately 1% (7%) of the pions (kaons) decay before triggering the detector.

G. Transverse-momentum resolution

High-mass dimuon data taken concurrently with these data using a short (5.6 cm), thin beryllium target yielded a mass resolution of 0.022 GeV/c^2 for the upsilon[16] and was in good agreement with the momentum scale determined from magnetic field measurements to this accuracy. The calculated resolution in p_T for single hadrons ($\sigma_{p_T}/p_T \approx 2.4\%$) was somewhat worse than the upsilon resolution due to the longer liquid target and the angular divergence of the beam of approximately 0.68 mrad (rms) in the vertical direction, which affects the single-particle p_T but not the diparticle invariant mass.

H. Track-reconstruction background

Tracks were selected by a series of cuts on the reconstructed trajectory and the X and Y coordinates at the target Z plane. Two cuts were made on the trajectory inside the SM0-SM12 magnets.

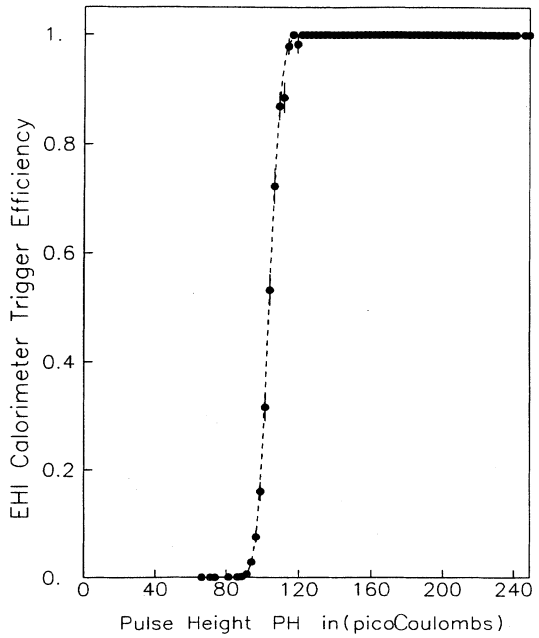

FIG. 4. The calculated efficiency of the *EHI* calorimeter trigger.

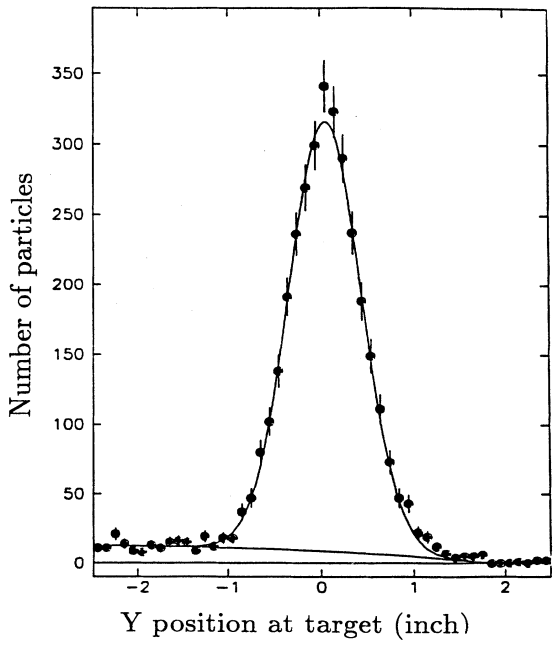

FIG. 5. The target Y distribution for positive particles showing the Gaussian and polynomial fits.

TABLE III. The calculated background fraction of the reconstructed target tracks.

Data set	Negative particles	Positive particles
800 GeV *pp*	0.041±0.003	0.038±0.002
400 GeV *pp* (norm)	0.071±0.018	0.074±0.009
400 GeV *pp* (rev)	0.096±0.024	0.096±0.024
400 GeV *pd*	0.033±0.004	0.104±0.006

One cut was made on the Y position at the downstream end of the low-angle collimator. The Y position of this aperture point was determined using high-mass electron-pair data.[17] Electrons provided an accurate guide to locate the collimator, because the tungsten collimator effectively absorbed all incident electrons. The second cut was performed at the Y position of the last lead-tungsten baffle in the SM12 magnet to remove tracks emerging from the steel of the magnet.

These cuts were made 2 standard deviations (according to the resolution of the track reconstruction) further into the aperture than the determined aperture points. Increasing these cuts to 5 standard deviations did not significantly change the measured cross sections or particle ratios.

Even with these trajectory cuts, some background events remained in the final target Y distribution. A fit to each distribution with a Gaussian and third-order polynomial yielded an estimate of this background. A cut was made at 4 (3) standard deviations of the fitted Gaussian for the 800- (400-) GeV/c data and the fitted background subtracted. Figure 5 shows the results of one such fit. Note that the width of the distribution is dominated by the tracking resolution and not the width of the incoming proton beam. The complete results are shown in Table III where the terms "norm" and "rev" refer to two separate 400-GeV/c data-taking periods when the

TABLE IV. The values of the single-positive- and -negative-pion inclusive invariant cross section per nucleus as a function of transverse momentum for (a) pp $\sqrt{s}=27.4$ GeV, (b) pd $\sqrt{s}=27.4$ GeV, and (c) pp $\sqrt{s}=38.8$ GeV. The data are averaged over the range in cosΘ^* given in Table I and the stated transverse-momentum bin. Each entry contains the measured cross section followed by the statistical and systematic uncertainty. The ± 2% systematic uncertainty in the *pd* cross sections due to the contamination of the "deuterium" target is not included in the entries in (b).

p_T bin (GeV/c)	$\langle p_T \rangle$ (GeV/c)	$[pb/(\text{GeV}^2/c^3)]$
	(a) pp $\sqrt{s}=27.4$ (GeV)	
		$E\frac{d^3\sigma}{dp^3}(pp\to\pi^-X)$
5.2–5.7	5.60	$(2.37\pm1.03\pm0.19)\times10^{1}$
5.7–6.2	5.97	$7.33\pm2.12\pm0.46$
6.2–6.7	6.35	$1.97\pm0.84\pm0.16$
		$E\frac{d^3\sigma}{dp^3}(pp\to\pi^+X)$
5.2–5.7	5.52	$(3.41\pm1.78\pm0.41)\times10^{1}$
5.7–6.2	5.95	$(1.53\pm0.31\pm0.09)\times10^{1}$
6.7–7.2	6.92	$1.05\pm0.56\pm0.09$
7.2–7.7	7.56	$(2.15\pm1.32\pm0.45)\times10^{-1}$
7.7–9.0	8.10	$(1.52\pm0.94\pm0.67)\times10^{-2}$
	(b) pd $\sqrt{s}=27.4$ Ge	
		$E\frac{d^3\sigma}{dp^3}(pp\to\pi^+X)$
5.2–5.7	5.57	$(8.73\pm2.12\pm0.58)\times10^{1}$
5.7–6.2	5.96	$(1.46\pm0.20\pm0.08)\times10^{1}$
6.2–6.7	6.44	$3.67\pm0.61\pm0.23$
6.7–7.2	6.83	$1.16\pm0.32\pm0.08$
7.2–7.7	7.43	$(4.60\pm1.07\pm0.30)\times10^{-1}$
7.7–9.0	8.04	$(1.66\pm0.40\pm0.30)\times10^{-2}$
		$E\frac{d^3\sigma}{dp^3}(pp\to\pi^+X)$
5.2–5.7	5.57	$(7.87\pm1.56\pm0.77)\times10^{1}$
5.7–6.2	5.95	$(2.15\pm0.24\pm0.13)\times10^{1}$
6.2–6.7	6.41	$7.07\pm0.90\pm0.47$
6.7–7.2	7.02	$(9.23\pm3.29\pm0.98)\times10^{-1}$

p_T bin (GeV/c)	$\langle p_T \rangle$ (GeV/c)	$[pb/(\text{GeV}^2/c^3)]$
	(b) pd $\sqrt{s}=27.4$ Ge	
		$E\frac{d^3\sigma}{dp^3}(pp\to\pi^+X)$
7.2–7.7	7.46	$(4.77\pm0.87\pm0.27)\times10^{-1}$
7.9–9.0	8.13	$(2.97\pm0.64\pm0.61)\times10^{-2}$
	(c) pp $\sqrt{s}=38.8$ GeV	
		$E\frac{d^3\sigma}{dp^3}(pp\to\pi^+X)$
3.6–4.0	3.87	$(1.00\pm0.18\pm0.08)\times10^{4}$
4.0–4.5	4.23	$(3.26\pm0.27\pm0.24)\times10^{3}$
4.5–5.0	4.71	$(9.92\pm0.83\pm0.77)\times10^{2}$
5.0–5.5	5.17	$(2.83\pm0.31\pm0.27)\times10^{2}$
5.5–6.0	5.63	$(1.06\pm0.14\pm0.09)\times10^{2}$
6.0–6.5	6.29	$(3.58\pm0.78\pm0.31)\times10^{1}$
7.0–7.5	7.22	$1.85\pm0.68\pm0.16$
7.5–8.0	7.71	$1.60\pm0.44\pm0.12$
8.0–9.0	8.50	$(4.52\pm1.73\pm0.43)\times10^{-1}$
		$E\frac{d^3\sigma}{dp^3}(pp\to\pi^+X)$
3.6–4.0	3.89	$(1.62\pm0.33\pm0.13)\times10^{4}$
4.0–4.5	4.23	$(4.62\pm0.38\pm0.33)\times10^{3}$
4.5–5.0	4.73	$(1.40\pm0.12\pm0.11)\times10^{3}$
5.0–5.5	5.20	$(4.42\pm0.40\pm0.39)\times10^{2}$
5.5–6.0	5.64	$(1.66\pm0.19\pm0.14)\times10^{2}$
6.0–6.5	6.14	$(5.87\pm0.88\pm0.45)\times10^{1}$
6.5–7.0	6.64	$(1.35\pm0.16\pm0.08)\times10^{1}$
7.0–7.5	7.26	$5.72\pm0.81\pm0.36$
7.5–8.0	7.82	$2.64\pm0.68\pm0.16$
8.0–9.0	8.44	$(6.78\pm1.87\pm0.58)\times10^{-1}$
9.0–11.0	9.65	$(5.87\pm4.20\pm1.00)\times10^{-2}$

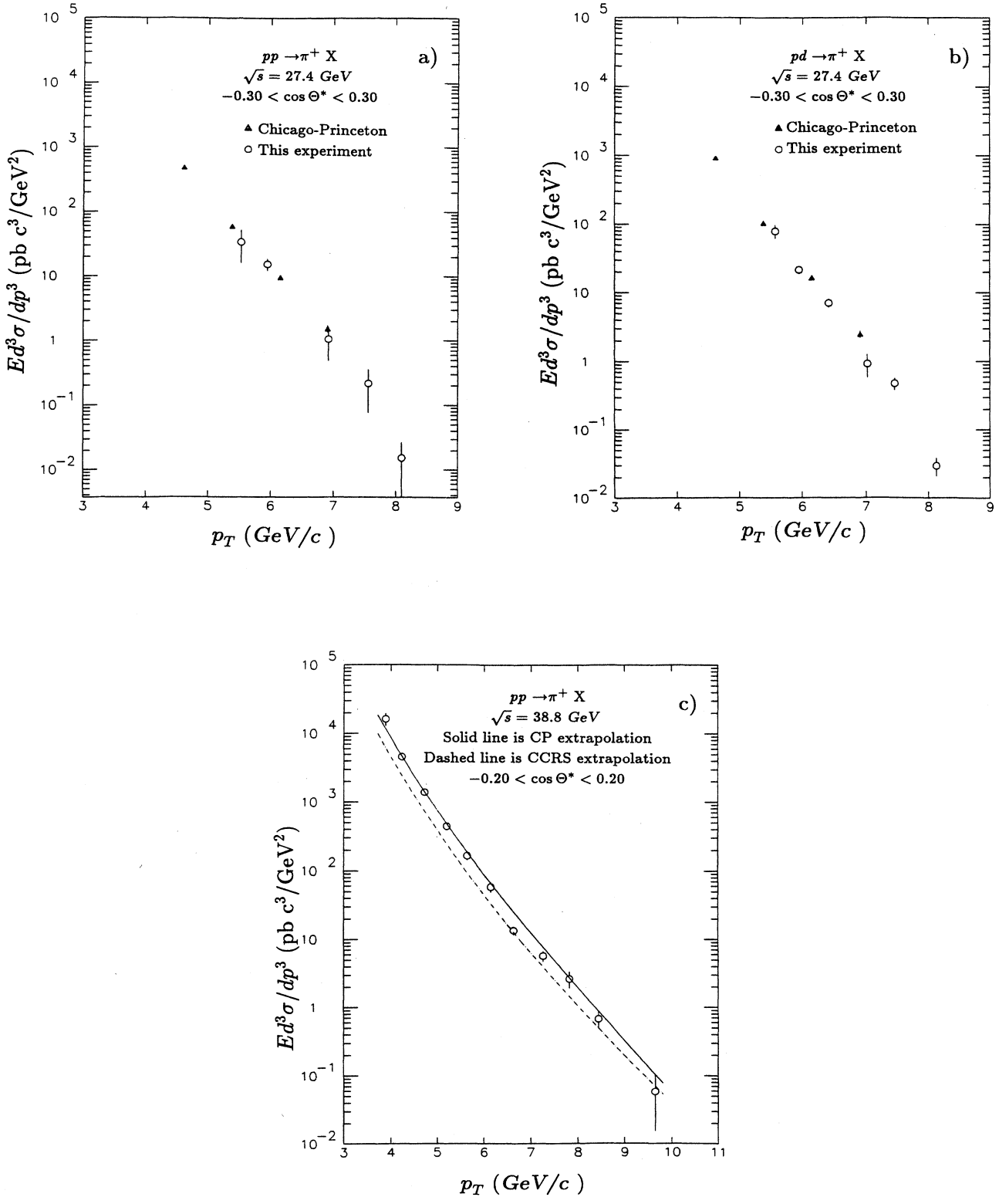

FIG. 6. The single-positive-pion inclusive invariant cross sections per nucleus as a function of transverse momentum for (a) $pp\sqrt{s}=27.4$ GeV, (b) $pd\ \sqrt{s}=27.4$ GeV, and (c) $pp\ \sqrt{s}=38.8$ GeV. The ± 2% systematic uncertainty in the pd cross sections due to target contamination is not included in (b).

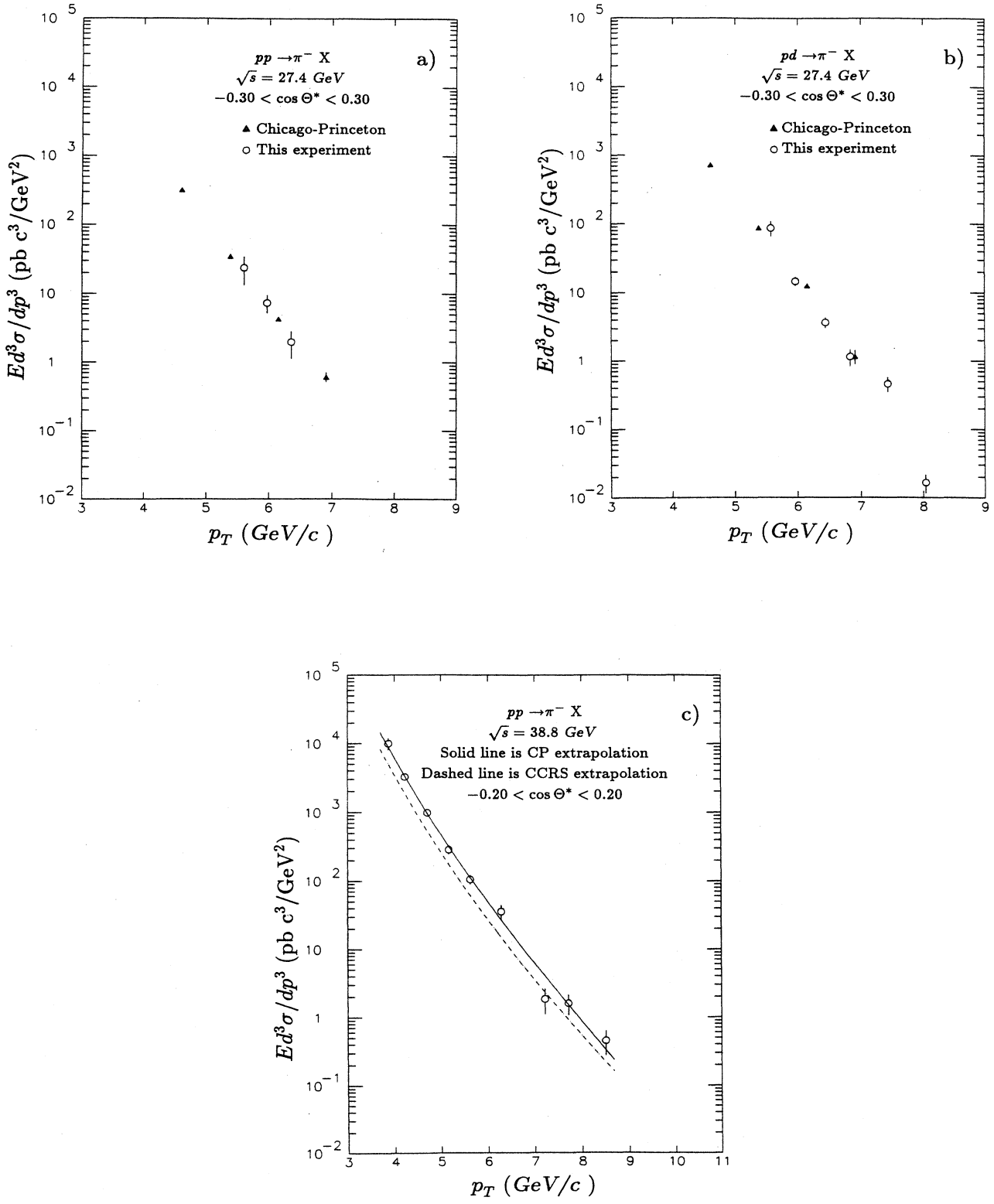

FIG. 7. The single-negative-pion inclusive invariant cross sections per nucleus as a function of transverse momentum for (a) pp $\sqrt{s}=27.4$ GeV, (b) pd $\sqrt{s}=27.4$ GeV, and (c) pp $\sqrt{s}=38.8$ GeV. The $\pm 2\%$ systematic uncertainty in the pd cross sections due to target contamination is not included in (b).

polarities of spectrometer magnets were reversed as a systematic check.

III. SINGLE-PION CROSS SECTIONS

The invariant cross sections

$$\left\langle E\frac{d^3\sigma}{dp^3}\right\rangle \equiv \int E\frac{d^3\sigma}{dp^3}\frac{d^3p}{E}\Big/\int\frac{d^3p}{E}\ ,$$

for inclusive single-pion production averaged over each c.m.s. bin are given in Table IV. Each entry in the table gives the width of the p_T bin, the weighted mean transverse momentum

$$\langle p_T\rangle \equiv \int p_T E\frac{d^3\sigma}{dp^3}\frac{d^3p}{E}\Big/\int E\frac{d^3\sigma}{dp^3}\frac{d^3p}{E}$$

in each bin and the measured cross section with the statistical and systematic uncertainty. Entries are omitted when the measurement is not significantly different from zero at one standard deviation. Figures 6 and 7 show the cross sections for π^+ and π^-, respectively, plotted versus $\langle p_T\rangle$; the errors shown in the figures are the statistical and systematic uncertainty added in quadrature. Note that the transverse momentum that corresponds to the measured average cross section is not identical to $\langle p_T\rangle$; however, the difference is estimated by Monte Carlo methods to be less than 0.13 GeV/c for all the measurements shown and does not appreciably affect the shape of the cross section versus p_T.

Shown for comparison at $\sqrt{s}=27.4$ GeV are the results of the Chicago-Princeton (CP) Collaboration[2] obtained at $\langle\Theta^*\rangle=96°$. In addition extrapolations of the charged-pion cross-section measurements of the CP and CERN-Columbia-Rockefeller-Saclay[3] (CCRS) Collaborations based on fits of the form $E\,d^3\sigma/dp^3=Af(x_T)p_T^{-N}$ are shown with the measurements of this experiment at $\sqrt{s}=38.8$ GeV.

All results confirm the steep dependence of the single-pion cross section on p_T. The lower-energy cross sections for both π^+ and π^- in pp and pd collisions show very good agreement with the CP measurements where the measurements overlap while the $\sqrt{s}=38.8$ GeV pp cross sections are consistent with the CP extrapolation and systematically higher than the CCRS fit.

In the naive parton model, N was predicted to be 4 (Ref. 18), but experiments[2,3] have measured $N\approx 8$ thus motivating a QCD-based description of high-p_T inclusive hadron production. The resulting QCD-improved parton model (incorporating the Q^2 dependence of the strong coupling, structure functions, and fragmentation functions and the intrinsic transverse momentum of the partons in the nucleon) agreed with the measured single-pion cross sections for the existing data.[19,20] In addition, N was predicted to decrease at fixed x_T as $\sqrt{s}$ increases in inclusive single-hadron production[20] and N was expected to be less than 8 in inclusive single-jet production. Jet measurements at the ISR and the CERN p-$\bar{p}$ collider indicated $N=5.3\pm0.2$ (Ref. 21) and inclusive π^0 production for $x_T>0.3$ were consistent with $N\approx 6$ (Ref. 22). The predicted and measured scale-dependent variation of N diminishes the ability of the scaling form $Af(x_T)p_T^{-N}$ to parametrize $E\,d^3\sigma/dp^3$ over a large range in p_T or $\sqrt{s}$; nevertheless, it is a convenient form that facilitates comparison to other experiments.

The results of fits to the proton-proton data over the entire x_T range ($0.19<x_T<0.66$) to the scaling form $E\,d^3\sigma/dp^3=Af(x_T)p_T^{-N}$ for two forms of $f(x_T)$ are shown in Table V. Also shown in the table are the results of the fits by CP and CCRS to their data. Only the diagonal elements of the error matrix are shown for the fits to the measurements of this experiment. There is, however, a strong correlation between b and N, perhaps due to only two values of $\sqrt{s}$ (27.4 and 38.8 GeV) available to this experiment compared to the three values used by CP (19.4, 23.8, and 27.4 GeV) and CCRS (44.8, 52.7, and 62.4 GeV). Both fits give similar values of N for π^+ and π^- production and show an almost identical dependence on p_T as observed by CCRS or CP. Fits restricted to a high-x_T range ($x_T>0.35$) did not yield significantly different results for N contrary to the results of Ref. 22.

TABLE V. The values of the fit parameters b and N for the invariant cross section per nucleus for positive and negative pions for this experiment, Ref. 2 (CP), and Ref. 3 (CCRS). The functional form of the fit is $E\,d^3\sigma/dp^3=Af(x_T)p_T^{-N}$ where two forms of $f(x_T)$ were used to facilitate comparison between experiments. The tables show the range in x_T over which the cross section was fit by each experiment. In the table $N_{\rm DF}$ means number of degrees of freedom.

$f(x_T)$	b	N	$\chi^2/N_{\rm DF}$	
	This experiment ($0.19<x_T<0.66$)			
$(1-x_T)^b$	10.8±0.3	8.4±0.1	16.1/13	π^+
$(1-x_T)^b$	10.6±0.6	8.4±0.1	9.4/9	π^-
	CP Collaboration ($0.35<x_T<0.64$)			
$(1-x_T)^b$	9.0±0.5	8.2±0.5	17/8	π^+
$(1-x_T)^b$	9.5±0.5	8.5±0.5	5.8/7	π^-
	This experiment ($0.19<x_T<0.66$)			
e^{-bx_T}	20.4±0.4	7.0±0.1	21.5/13	π^+
e^{-bx_T}	17.2±1.0	7.7±0.2	10.4/9	π^-
	CCRS Collaboration ($0.11x_T<0.36$)			
e^{-bx_T}	15.4±1.2	7.5±0.17	72/63	π^+
e^{-bx_T}	16.1±1.2	7.86±0.30	70/64	π^-

IV. PARTICLE RATIOS

Tables VI, VII, and VIII contain the K/π and p/π production ratios and particle fractions for $\sqrt{s}=27.4$ GeV pp, $\sqrt{s}=27.4$ GeV pd, and $\sqrt{s}=38.8$ GeV pp interactions, respectively. Each table entry gives the p_T bin width and the measured particle ratio along with the statistical and estimated systematic uncertainty—only statistical errors are shown in Figs. 8–12.

A. K^+/π^+ ratio

In Figs. 8(a), 8(b), and 8(c), the K^+/π^+ ratios measured in $\sqrt{s}=27.4$-GeV pp and pd collisions and

$\sqrt{s}=38.8$-GeV pp collisions in this experiment are shown. The results of the CP experiment[2] and the predictions of the Lund model[23] are shown for comparison. The lower-energy measurements of both experiments are consistent in the region of overlap; however, the Lund predictions are systematically lower than the measurements.

As noted previously,[24] the roughly constant value of the K^+/π^+ ratio for $p_T>3$ GeV/c should reflect the relative probability that a valence u quark picks up an s or d quark, $P(s)/P(d)$, in the fragmentation process. A comparison of the average values of the K^+/π^+ ratio for $p_T>3$ GeV/c as measured in this experiment and predicted by the Lund model is shown in Table IX. One possible explanation of the discrepancy is that pion production by resonance decay is inadequately modeled by the Lund model.[25] Another possibility[26] is that the standard Lund parameters correctly model the fragmentation process at low z (Ref. 27) but begin to fail as z increases above ≈ 0.25. The measurements of $e^+e^-\rightarrow$ hadrons used to develop the Lund parameters are dominated by a cross section that falls steeply as z increases. On the other hand, high-p_T hadrons have been shown[1] to have $\langle z\rangle \approx 0.8$; therefore, high-transverse-momentum hadrons probe a region in the fragmentation process poorly examined in electron-positron collisions.

Figure 8(d) and Table IX compare the measurements at $\sqrt{s}=27.4$ and 38.8 GeV in pp collisions to predictions by the Split Field Magnet (SFM) Collaboration's Monte Carlo simulation package.[28] The SFM Monte Carlo program (described in detail in Refs. 5, 24, and 29) parametrizes fragmentation distributions generated by the Lund Monte Carlo program at a fixed jet momentum of 10 GeV/c. Three standard Lund features were changed for the SFM predictions: (1) $P(s)/P(d)=0.45$, (2) $P(qq)/P(q)=0.09$, and (3) gluons fragment into quark-antiquark pairs that fragment independently. The calculations were performed for pp collisions at $\sqrt{s}=39$ GeV at a production angle of 90°. The agreement is excellent, despite the extrapolation required from the angu-

TABLE VI. The particle ratios (a) and fractions (b) as a function of transverse momentum for the pp $\sqrt{s}=27.4$-GeV data. Each entry in (a) contains the measured particle ratio, the statistical and systematic error. Each entry in (b) contains the measured particle fraction, the statistical and systematic error. The sign of the systematic uncertainty reflects the correlation between the three particle fractions (each hadron is either a π, K, or p).

(a)

p_T bin (GeV/c)	K^+/π^+	p/π^+
5.2–5.7	0.418±0.058±0.003	0.226±0.042±0.006
5.7–6.2	0.423±0.037±0.007	0.236±0.027±0.004
6.2–6.7	0.407±0.047±0.008	0.133±0.029±0.004
6.7–7.2	0.383±0.061±0.017	0.087±0.033±0.023
7.2–7.7	0.487±0.127±0.021	0.208±0.076±0.011
7.7–9.0	0.725±0.248±0.230	
	K^-/π^-	$\bar{p}/\pi^-$
5.2–5.7	0.114±0.034±0.002	0.165±0.043±0.005
5.7–6.2	0.125±0.024±0.005	0.085±0.024±0.003
6.2–6.7	0.081±0.025±0.007	0.042±0.026±0.003
6.7–7.2	0.095±0.044±0.014	
7.2–7.7	0.058±0.055±0.014	0.608±0.058±0.007

(b)

p_T bin (GeV/c)	π^+/h^+	K^+/h^+	p/h^+
5.2–5.7	0.608±0.040∓0.002	0.254±0.030∓0.000	0.137±0.023±0.002
5.7–6.2	0.603±0.025∓0.002	0.255±0.019±0.002	0.142±0.015∓0.000
6.2–6.7	0.649±0.036∓0.003	0.264±0.026±0.003	0.086±0.018±0.000
6.7–7.2	0.680±0.051±0.004	0.260±0.035±0.007	0.060±0.022∓0.011
7.2–7.7	0.590±0.080∓0.006	0.287±0.060±0.006	0.123±0.041∓0.000
7.7–9.0	0.565±0.115∓0.061	0.410±0.103±0.068	0.025±0.051∓0.007
	π^-/h^-	K^-/h^-	$\bar{p}/h^-$
5.2–5.7	0.782±0.061∓0.002	0.089±0.025∓0.000	0.129±0.030±0.002
5.7–6.2	0.826±0.043∓0.002	0.104±0.019±0.002	0.071±0.019∓0.000
6.2–6.7	0.891±0.063∓0.003	0.072±0.022±0.003	0.037±0.023∓0.000
6.7–7.2	0.910±0.101±0.006	0.086±0.038±0.007	0.004±0.040∓0.013
7.2–7.7	0.888±0.161∓0.006	0.052±0.047±0.006	0.060±0.049∓0.000
7.7–9.0	0.655±0.287∓0.056	0.184±0.180±0.062	0.161±0.157∓0.006

lar region, $\Theta^* \leq 50°$, where the SFM group measured hadroproduction.

B. p/π^+ ratio

The p/π^+ ratios for $\sqrt{s}=27.4$ GeV pp and pd collisions are shown in Figs. 9(a) and 9(b) along with the CP data and Lund predictions. Again there is good agreement with CP and disagreement with the consistently higher predictions of the Lund program. When the $pp \rightarrow p/\pi^+$ data at both $\sqrt{s}=27.4$ and 38.8 GeV are plotted versus the scaling variable x_T, as in Fig. 10(a), the nonscaling behavior of the ratio is observed, in accordance with the supposition[30] that proton production arises from constituent diquark scattering and exhibits the Q^2 dependence of the diquark form factor. This hypothesis is strengthened by the better agreement of the ratios when plotted versus p_T as in Fig. 10(b), if it is supposed that $p_T^2 \propto Q^2$.

In Fig. 10(c) the SFM calculation is compared to the data. The dominant source of protons in this calculation is rank-1 fragmentation of quarks. (A "rank-1" parton is a parton from the primary interaction vertex. "Rank-2" partons are produced in the fragmentation of "rank-1" partons.) The predicted p/π^+ ratio depends directly on two phenomenological parameter inputs: the probability of a gluon to fragment to a baryon (or antibaryon) and the probability of a quark (antiquark) to fragment to a baryon (antibaryon). These parameters were set to values of 0.003 and 0.09 for the calculation shown. Eighty percent of the protons are produced in quark fragmentation. No constituent diquark contribution was calculated which explains the inability of the model to describe the p/π^+ ratio at low p_T.

C. K^-/π^- ratio

The $\sqrt{s}=27.4$-GeV measurements of K^-/π^- vs p_T shown in Figs. 11(a) and 11(b) are generally compatible with CP measurements and the Lund simulation. When the $\sqrt{s}=27.4$- and 38.8-GeV $pp \rightarrow K^-/\pi^-$ measurements are plotted versus x_T as in Fig. 12(a) the x dependence of the gluon structure function (times the ratio of the fragmentation functions)—generally considered to be the source of K^- at low p_T (Ref. 24)—is visible. Comparison with the SFM Monte Carlo simulation in Fig.

TABLE VII. The particle ratios (a) and fractions (b) as a function of tranverse momentum for the pd $\sqrt{s}=27.4$-GeV data.

(a)

p_T bin (GeV/c)	$K^+/\pi+$	p/π^+
5.2–5.7	0.440±0.068±0.003	0.161±0.045±0.006
5.7–6.2	0.418±0.033±0.025	0.132±0.021±0.014
6.2–6.7	0.369±0.035±0.006	0.140±0.023±0.003
6.7–7.2	0.374±0.036±0.016	0.108±0.019±0.021
7.2–7.7	0.391±0.050±0.019	0.089±0.025±0.009
7.7–9.0	0.429±0.088±0.186	0.146±0.048±0.098
	K^-/π^-	$\bar{p}/\pi^-$
5.2–5.7	0.079±0.017±0.002	0.066±0.020±0.004
5.7–6.2	0.092±0.012±0.005	0.067±0.014±0.003
6.2–6.7	0.084±0.015±0.006	0.023±0.014±0.003
6.7–7.2	0.078±0.018±0.011	
7.2–7.7	0.028±0.016±0.013	

(b)

p_T bin (GeV/c)	π^+/h^+	K^+/h^+	p/h^+
5.2–5.7	0.625±0.049∓0.002	0.275±0.036∓0.000	0.100±0.026±0.002
5.7–6.2	0.645±0.025∓0.007	0.270±0.018±0.009	0.085±0.013∓0.002
6.2–6.7	0.663±0.030∓0.002	0.245±0.020±0.002	0.092±0.014±0.000
6.7–7.2	0.675±0.032±0.003	0.252±0.021±0.007	0.073±0.013∓0.011
7.2–7.7	0.676±0.043∓0.006	0.264±0.028±0.006	0.060±0.016∓0.000
7.7–9.0	0.635±0.068∓0.056	0.272±0.046±0.062	0.093+0.029∓0.006
	π^-/h^-	K^-/h^-	$\bar{p}/h^-$
5.2–5.7	0.873±0.042∓0.002	0.069±0.014∓0.000	0.057±0.017±0.002
5.7–6.2	0.863±0.028∓0.002	0.079±0.010±0.002	0.058±0.011∓0.000
6.2–6.7	0.903±0.039∓0.003	0.076±0.013±0.002	0.021±0.012±0.000
6.7–7.2	0.920±0.048±0.003	0.072±0.016±0.007	0.007±0.014∓0.010
7.2–7.7	0.968±0.073∓0.006	0.027±0.015±0.006	0.004±0.017∓0.000
7.7–9.0	0.931±0.138∓0.059	0.028±0.029±0.066	0.041±0.040∓0.007

TABLE VIII. The particle ratios (a) and fractions (b) as a function of transverse momentum for the pp $\sqrt{s}=38.8$-GeV data.

(a)

p_T bin (GeV/c)	K^+/π^+	p/π^+
3.6–4.0	0.530±0.041±0.014	0.355±0.030±0.010
4.0–4.5	0.481±0.023±0.013	0.206±0.016±0.009
4.5–5.0	0.470±0.034±0.005	0.163±0.022±0.003
5.0–5.5	0.559±0.057±0.004	0.110±0.029±0.004
5.5–6.0	0.433±0.045±0.006	0.105±0.023±0.004
6.0–6.5	0.484±0.036±0.007	0.084±0.014±0.004
6.5–7.0	0.467±0.035±0.019	0.050±0.011±0.011
7.0–7.5	0.562±0.051±0.036	0.095±0.018±0.023
7.5–8.0	0.447±0.050±0.033	0.053±0.015±0.017
8.0–9.0	0.453±0.051±0.112	0.064±0.017±0.058
9.0–11.0	0.494±0.099±0.147	0.021±0.015±0.075
	K^-/π^-	$\bar{p}/\pi^-$
3.6–4.0	0.296±0.029±0.010	0.063±0.021±0.007
4.0–4.5	0.279±0.019±0.010	0.051±0.014±0.007
4.5–5.0	0.270±0.027±0.004	
5.0–5.5	0.175±0.029±0.003	0.030±0.017±0.003
5.0–6.0	0.172±0.029±0.004	
6.0–6.5	0.138±0.023±0.001	0.016±0.009±0.001
6.5–7.0	0.104±0.022±0.014	
7.0–7.5	0.145±0.032±0.026	
7.5–8.0	0.081±0.026±0.039	0.033±0.016±0.020
8.0–9.0	0.087±0.031±0.084	
9.0–11.0	0.061±0.049±0.103	

(b)

p_T bin (GeV/c)	π^+/h^+	K^+/h^+	p/h^+
3.6–4.0	0.531±0.022∓0.004	0.281±0.018±0.003	0.188±0.014±0.001
4.0–4.5	0.593±0.015∓0.004	0.285±0.012±0.003	0.122±0.009±0.001
4.5–5.0	0.612±0.022∓0.001	0.288±0.017±0.002	0.100±0.013∓0.000
5.0–5.5	0.599±0.034∓0.002−	0.335±0.027±0.000	0.066±0.017±0.000
5.5–6.0	0.650±0.035∓0.002	0.281±0.024±0.002	0.068±0.014∓0.000
6.0–6.5	0.638±0.026∓0.002	0.309±0.019±0.003	0.054±0.009∓0.001
6.5–7.0	0.659±0.027∓0.005	0.308±0.019±0.007	0.033±0.007∓0.002
7.0–7.5	0.604±0.031∓0.012	0.339±0.024±0.010	0.057±0.010±0.002
7.5–8.0	0.667±0.038∓0.011	0.298±0.027±0.011	0.035±0.010±0.000
8.0–9.0	0.659±0.037∓0.035	0.299±0.027±0.039	0.042±0.011∓0.003
9.0–11.0	0.660±0.067∓0.047	0.326±0.051±0.050	0.014±0.010∓0.002
	π^-/h^-	K^-/h^-	$\bar{p}/h^-$
3.6–4.0	0.736±0.030∓0.004	0.218±0.019±0.003	0.047±0.015±0.001
4.0–4.5	0.752±0.021∓0.004	0.210±0.013±0.003	0.038±0.010±0.001
4.5–5.0	0.779±0.032∓0.001	0.210±0.019±0.002	0.011±0.015∓0.000
5.0–5.5	0.830±0.049∓0.002	0.145±0.022±0.000	0.025±0.014±0.000
5.5–6.0	0.853±0.049∓0.001	0.146±0.023±0.002	0.001±0.022∓0.000
6.0–6.5	0.867±0.045±0.000	0.119±0.018±0.000	0.014±0.008∓0.000
6.5–7.0	0.900±0.050∓0.005	0.094±0.018±0.007	0.007±0.007∓0.002
7.0–7.5	0.873±0.059∓0.012	0.126±0.026±0.010	0.001±0.023±0.002
7.5–8.0	0.898±0.065∓0.018	0.073±0.022±0.017	0.029±0.015±0.000
8.0–9.0	0.913±0.065∓0.037	0.080±0.027±0.040	0.007±0.016∓0.004
9.0–11.0	0.940±0.127∓0.047	0.057±0.045±0.050	0.003±0.028∓0.002

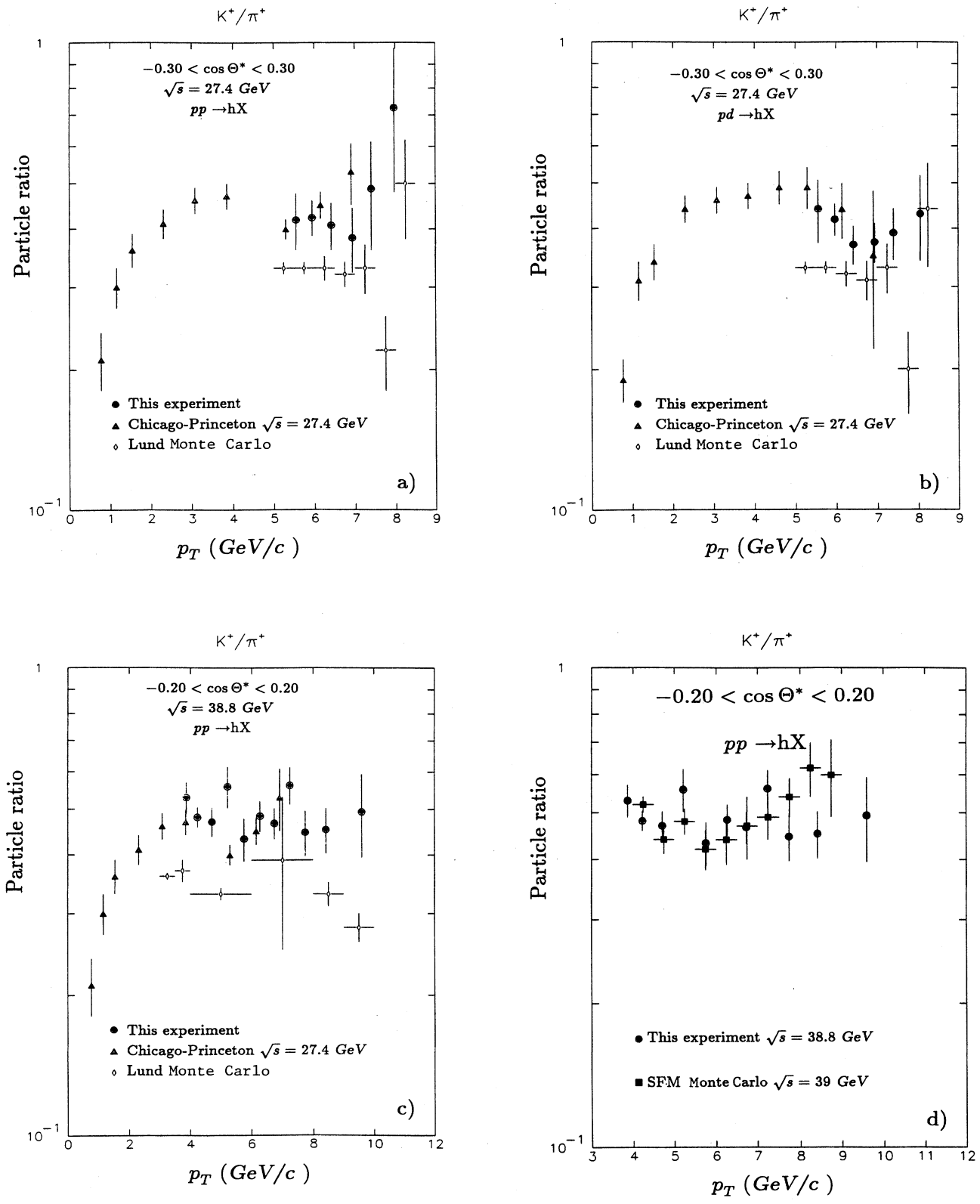

FIG. 8. The relative K^+/π^+ production rate as a function of transverse momentum for (a) pp $\sqrt{s}=27.4$ GeV , (b) pd $\sqrt{s}=27.4$ GeV, (c) pp $\sqrt{s}=38.8$ GeV, and (d) the measured relative K^+/π^+ production rate at $\sqrt{s}=38.8$ GeV compared to the SFM Monte Carlo simulation. The horizontal error bars show the bin width used for the Monte Carlo points.

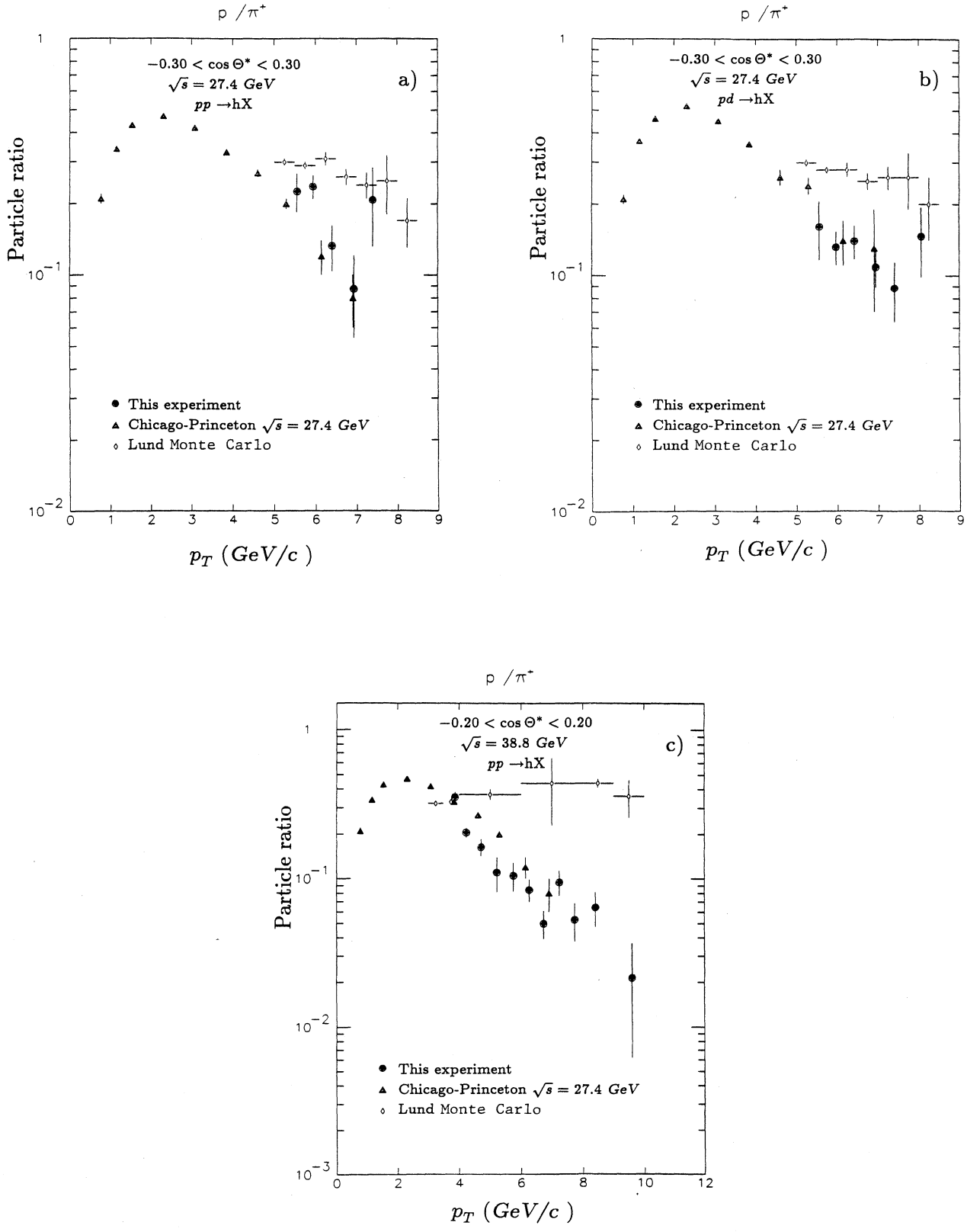

FIG. 9. The relative p/π^+ production rate as a function of transverse momentum for (a) pp $\sqrt{s}=27.4$ GeV, (b) pd $\sqrt{s}=27.4$ GeV, and (c) pp $\sqrt{s}=38.8$ GeV.

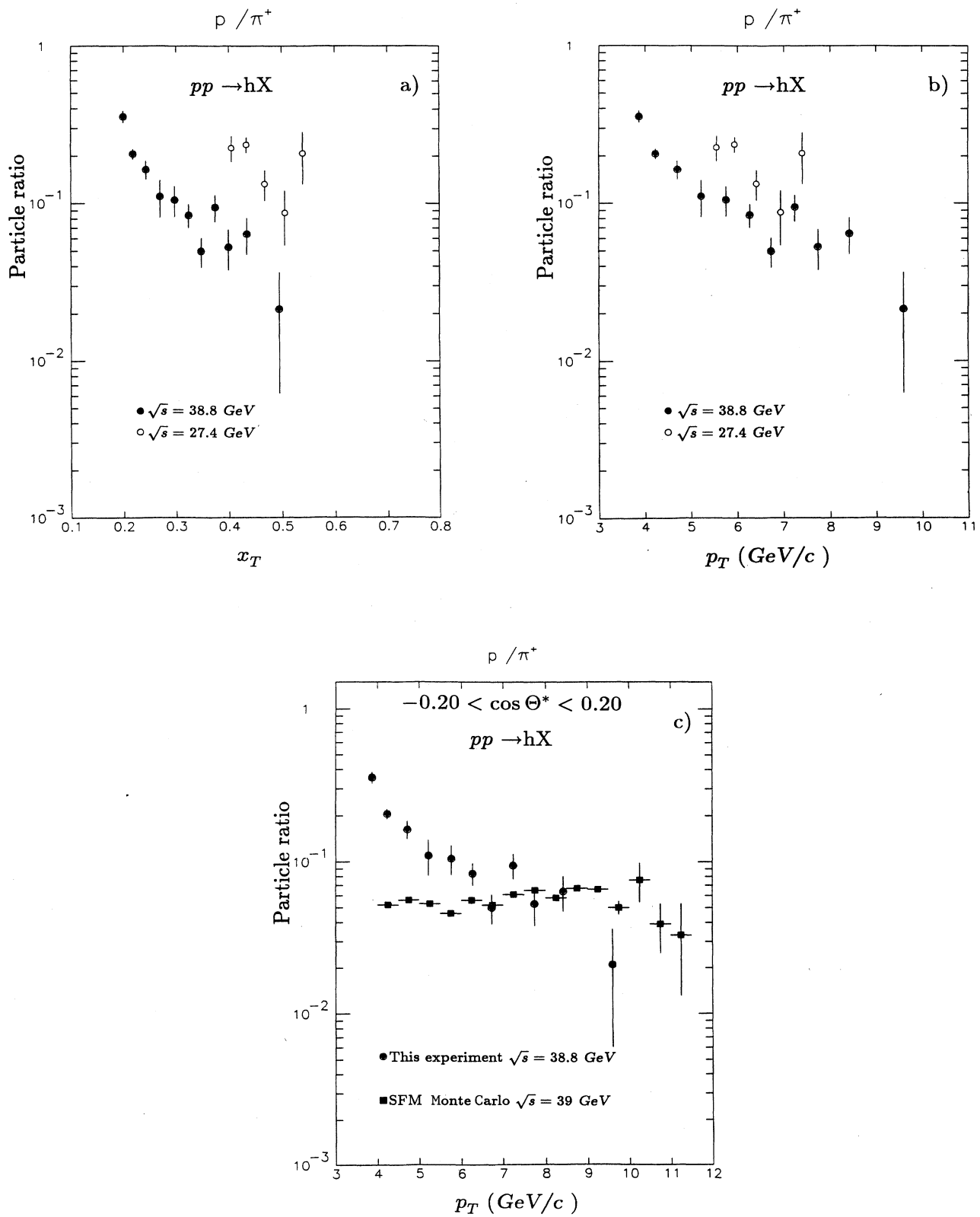

FIG. 10. The relative p/π^+ production rate in pp collisions as a function of (a) the scaled transverse momentum, (b) the transverse momentum, and (c) the transverse momentum at $\sqrt{s}=38.8$ GeV compared to the SFM Monte Carlo simulation.

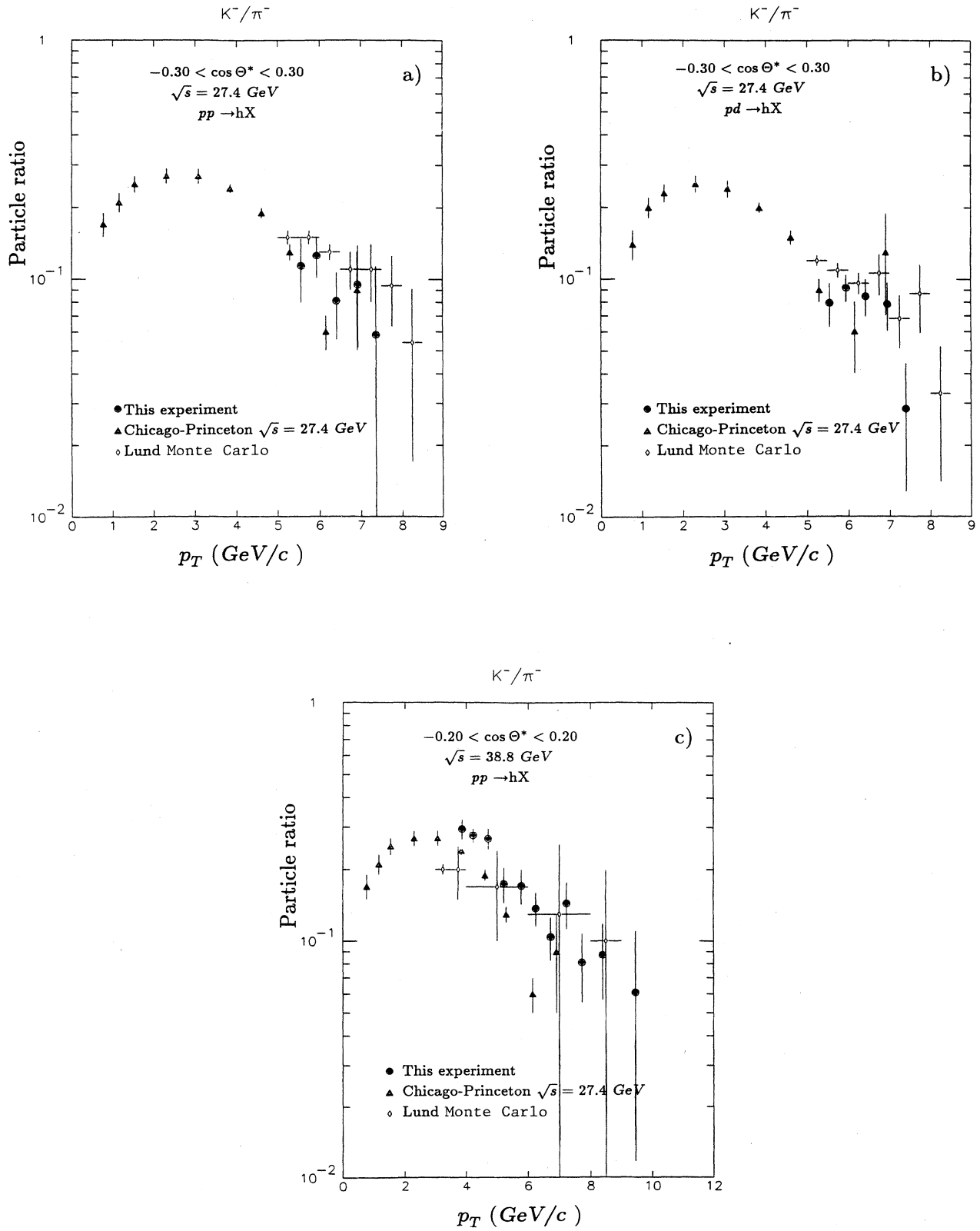

FIG. 11. The relative K^-/π^- production rate as a function of transverse momentum for (a) pp $\sqrt{s}$ =27.4 GeV, (b) pd $\sqrt{s}$ =27.4 GeV, and (c) pp $\sqrt{s}$ =38.8 GeV.

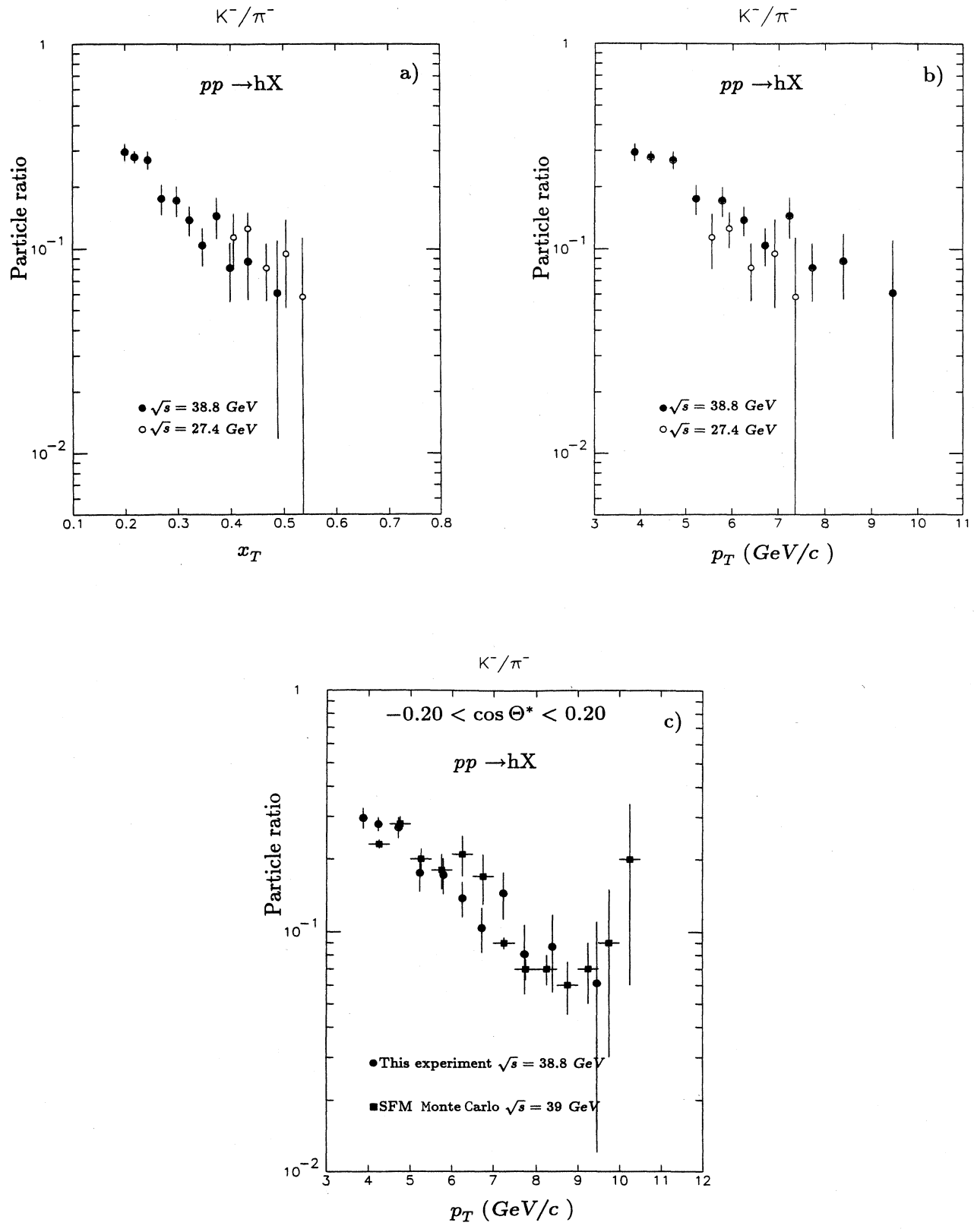

FIG. 12. The relative K^-/π^- production rate in pp collisions as a function of (a) the scaled transverse momentum, (b) the transverse momentum, and (c) the transverse momentum at $\sqrt{s}=38.8$ GeV compared to the SFM Monte Carlo simulation.

TABLE IX. Comparison of the measured and predicted K^+/π^+ ratio with statistical uncertainties only for $p_T > 3$ GeV/c.

Reaction (GeV)	This experiment	Lund prediction	SFM prediction
pp $\sqrt{s}=27.4$	0.47±0.06	0.32±0.02	
pd $\sqrt{s}=27.4$	0.40±0.04	0.32±0.02	
pp $\sqrt{s}=38.8$	0.49±0.04	0.33±0.02	0.49±0.04

12(c) shows good agreement in both shape and magnitude. The data span a kinematic region where the importance of rank-2 quark fragmentation in the production of K^- is increasing relative to rank-1 gluon fragmentation. According to the SFM Monte Carlo simulation, the percentage contribution of these sources—rank-1 gluon fragmentation:rank-1 quark fragmentation:rank-2 quark fragmentation:other—in K^- production are 60:10:25:5 for $x_T > 0.21$ and 40:8:45:7 for $x_T > 0.36$.

V. SUMMARY OF CONCLUSIONS

(1) The inclusive pion production cross sections show a similar steep dependence on p_T as seen by other experiments and parametrized by $E\,d^3\sigma/dp^3 = Af(x_T)p_T^{-N}$ with $N \approx 8$. No reduction in N was observed for the cross sections restricted to high x_T ($x_T > 0.35$).

(2) For $p_t > 3$ GeV/c, the constant value of the K^+/π^+ ratio shows the probability of a struck u quark to pick up an s or d quark in the fragmentation process. Good agreement with the predictions of the SFM Monte Carlo simulation is found, while comparison with the Lund Monte Carlo simulation reveals some possible inadequacies in the model.

(3) The nonscaling behavior of the p/π^+ ratio demonstrates the Q^2 dependence of the form factor of constituent diquarks.

(4) Comparison of the K^-/π^- ratio with the SFM Monte Carlo predictions shows the importance of K^- production by quark-gluon scattering.

ACKNOWLEDGMENTS

We would like to thank D. Drijard of CERN for providing the SFM calculations. In addition, we wish to thank Jim Peifer and the Fermilab liquid target group who fabricated and maintained the liquid targets. This work was supported in part by the U.S. Department of Energy, the National Science Foundation, the Commissariat à l'Energie Atomique, and the Japan Ministry of Education, Science and Culture (Monbusho).

*Present address: University of Illinois at Chicago, Chicago, Illinois 60680.
†Present address: Physikalisches Institut der Universität Bonn, Nussallee 12, 5300 Bonn 1, Federal Republic of Germany.
‡Present address: Aerospace Corporation, El Segundo, California 90245.
§Present address: Falkiner High Energy Physics Department, School of Physics, University of Sydney, Sydney, New South Wales 2006, Australia.
**Present address: Fermilab, Batavia, Illinois 60510.
††Present address: Northern Illinois University, Dekalb, Illinois 60115.
‡‡Present address: High Technology Center, Boeing Electronics Co., P.O. Box 24969, MS7J-56, Seattle, Washington 98124-6269.
§§Present address: University of Arizona, Tucson, Arizona 85721.

[1]A. L. S. Angelis *et al.*, Nucl. Phys. **B209**, 284 (1975).
[2]D. Antreasyan *et al.*, Phys. Rev. D **19**, 764 (1979).
[3]F. W. Büsser *et al.*, Nucl. Phys. **B106**, 1 (1976).
[4]T. Åkesson *et al.*, Nucl. Phys. **B246**, 408 (1984).
[5]A. Breakstone *et al.*, Z. Phys. C **28**, 335 (1985).
[6]A. Andersson *et al.*, Phys. Rep. **97**, 31 (1983); H.-U. Bengtsson and G. Ingleman, CERN Report No. LUTP 84-3, Th. 3820, 1984 (unpublished); T. Sjöstrand, Comput. Phys. Communi. **27**, 243 (1982).
[7]M. Althoff *et al.*, Z. Phys. C **17**, 5 (1983); H. Aihara *et al.*, Phys. Rev. Lett. **53**, 2199 (1984); Ch. Berger *et al.*, Nucl. Phys. **B124**, 189 (1983); M. Derrick *et al.*, Phys. Lett. **158B**, 519 (1985); M. Derrick *et al.*, Phys. Rev. Lett. **54**, 2568 (1985); W. Bartel *et al.*, Phys. Lett. **104B**, 325 (1981); P. Baringer *et al.*, Report No. ANL-HEP-PR-85-121 1985 (unpublished).
[8]Particle Data Group, Report No. LBL-91, 1985 (unpublished).
[9]J. A. Crittenden *et al.*, Phys. Rev. D **34**, 2584 (1986).
[10]D. E. Jaffe *et al.*, Phys. Rev. D **38**, 1016 (1988).
[11]D. E. Jaffe, Ph.D. dissertation, SUNY at Stony Brook, 1987.
[12]Fermilab liquid target group, J. Peifer (private communication). The purity was determined by accurately weighing a known volume of the liquid.
[13]R. Bouclier *et al.*, Nucl. Instrum. Methods **205**, 403 (1983); Ph. Mangeot *et al.*, *ibid.* **216**, 79 (1983); M. Adams *et al.*, *ibid.* **217**, 237 (1983); G. Coutrakon, Ph.D. dissertation, SUNY at Stony Brook, 1982; H. D. Glass, Ph.D. dissertation, SUNY at Stony Brook, 1985.
[14]P. B. Straub, Ph.D. dissertation, University of Washington (in preparation).
[15]J. A. Crittenden, Ph.D. dissertation, Columbia University, 1986.
[16]R. Gray, Ph.D. dissertation, University of Washington, 1988.
[17]T. Yoshida *et al.*, Phys. Rev. D **39**, 3264 (1989).
[18]S. M. Berman, J. D. Bjorken, and J. B. Kogut, Phys. Rev. D **4**, 3388 (1971).
[19]J. M. Owens, E. Reya, and M. Glück, Phys. Rev. D **18**, 1501 (1978); A. P. Coutogouris, P. Gaskell, and S. Papadopoulos, *ibid.* **17**, 2314 (1978).
[20]R. P. Feynman, R. D. Field, and G. C. Fox, Phys. Rev. D **18**, 3320 (1978).
[21]T. Åkesson *et al.*, Phys. Lett. **123B**, 133 (1983).
[22]A. G. Clark *et al.*, Phys. Lett. **74B**, 267 (1978); A.L.S. Angelis *et al.*, *ibid.* **79B**, 505 (1978); C. Kourkoumelis *et al.*, Z. Phys. C **5**, 95 (1980).
[23]The standard PYTHIA version 4.2 and JETSET version 6.2 of the Lund program were used. In the figures the horizontal error bars of the Lund points show the bin width. In these versions the strangeness suppression factor, $P(s)/P(d)$ is 0.3 and the diquark suppression factor $P(qq)/P(q)$ is 0.1. To obtain the

Lund-model results for *pd* interactions, the predicted hadron production rates in *pn* and *pp* collisions was simply summed.

[24]A. Breakstone *et al.*, Phys. Lett. 135**B**, 510 (1984).

[25]A. Seiden, in *6th International Conference on Proton Antiproton Collider Physics,* Aachen, Germany, 1986, edited by K. Eggert, H. Faissner, and E. Radermacher (World Scientific, Singapore, 1987).

[26]G. D. Cowan, Ph.D. Dissertation, University of California, Report No. LBL-24715, 1988; TPC/Two-Gamma Collaboration, H. Aihara *et al.*, Phys. Rev. Lett. **61**, 1263 (1988).

[27]The fragmentation variable z is defined as the fraction of the parton momentum carried by the observed hadron. In electron-positron collisions this definition reduces to the ratio of the hadron momentum to the beam momentum.

[28]D. Drijard, CERN (private communication).

[29]D. Drijard *et al.*, Phys. Lett. **121B**, 433 (1983); A. Breakstone *et al., ibid.* **135B**, 505 (1984).

[30]S. Ekelin and S. Fredriksson, Phys. Lett. **149B**, 509 (1984).